IEEJ Journal of Industry Applications
Vol.5 No.2 pp.78–89 DOI: 10.1541/ieejjia.5.78

Paper

Use of MEMS Inertial Sensors for Performance Improvement of Low-cost Motion Control Systems

Roberto Oboe[*,**a)] Non-member, Riccardo Antonello[*] Non-member
Davide Pilastro[*] Non-member, Kazuaki Ito[***] Senior Member

(Manuscript received April 13, 2015, revised Sep. 23, 2015)

The performance of a motion control system depends on hardware capabilities, such as sensor resolution and actuator technology. For a certain plant, an amelioration in performance can often be achieved by using better sensors. This however may require a redesign of the system, as the new sensor may not fit into the existing plant. As for the actuators, many motion control systems using stepper motors exist; these stepper motors known for their high torque ripple and limited dynamic performance, especially in the presence of mechanical resonances of the driven load. A possible solution is to replace the actuator with a better one; however, this again may require a costly redesign of the plant. To improve the performance of existing plants with minimal invasive modifications, our group has developed a set of solutions, based on the use of low-cost MEMS inertial sensors, which can be easily placed on the system to be controlled. We will show the manner in which we used such sensors to develop new control strategies, to enhance the performance of existing sensors and actuators, without major modifications to the plant. This will be demonstrated through some examples taken from both laboratory and industrial applications.

Keywords: MEMS inertial sensors, motion control, low resolution position sensors

1. Introduction

High accuracy and fast motion control of industrial mechatronic systems (e.g. machine tools, inspection equipment, surface mounting equipment etc.) is a key factor in the improvement of manufacturing quality, needed to respond to the increasing demand for products with high reliability and perceived quality. Indeed, the achievable control performance heavily relies on hardware performance, such as sensor resolution, actuator technology and computational power, and the achievement of a certain goal may require the replacement of the whole manufacturing equipment or some of its components. In particular, a possible solution for the improvement of the positioning performance of outdated equipment could be to replace the existing low-resolution position sensors with higher resolution ones. This, however, may require the complete redesign of the system, as the new sensor may not fit in the available space of the existing plant. In such a case, a possible solution is the use of sophisticated hardware for encoder signal processing, as proposed in [(1)], where a smart time-stamping and selection of encoder events is used to virtually increase the resolution in position measurement. The cost of such solution, however, is related to the additional high performance hardware to be used. An alternative low cost solution is to resort to the use of estimators, capable of providing smooth estimates of the actual position and, in turn, better motion control quality. Significant results on this approach have been reported in [(2)(3)]. Among all the possible estimation techniques, those based on Kalman filters (KF) [(4)] have gained a lot of interest in those applications where there is a need to estimate velocity and position of a system with low resolution sensors [(5)–(7)].

In other scenarios, the use of low-cost stepper motors leads to a limited achievable motion speed, especially in presence of mechanical resonances, as this type of actuators introduces some torque ripple. Even with the use of better performing Hybrid Stepper Motors (HSM), combined with micro stepping in the current driving of the stator coils, it is not possible to achieve the complete reduction of the ripple and cogging torques in this type of actuators. The limitations in the use of HSM are even stronger when they are used to move load through a flexible mechanical transmission. This is a typical industrial scenario, in which the problem of the oscillations arising from the excitation of the mechanical resonance by various disturbances (including torque ripple) is usually addressed by severely limiting the overall dynamic performance. Again, a possible solution is the replacement of the actuator with another, with better characteristics, but this may require the complete or partial redesign of the plant.

To avoid all the above-mentioned redesigns and to improve the performance of the existing plants with minimally invasive modifications, our group has developed a set of solutions, based on the use of low-cost MEMS inertial sensors,

a) Correspondence to: Roberto Oboe. E-mail: roberto.oboe@unipd.it
* Department of Management and Engineering, University of Padova
Stradella San Nicola, 3, 36100 Vicenza, Italy
** Fondazione Ospedale San Camillo I.R.C.C.S., Via Alberoni 70-30126 Venezia-Lido, Italy
*** Department of Electrical and Electronic Engineering, National Institute of Technology, Toyota College
2-1, Eisei-cho, Toyota 471-8525, Japan

properly placed on the mechanical load to be controlled. In this paper, it will be shown how the use of such sensors allow the development of new control strategies, by means of which it is possible to enhance the performance of existing hardware, without resorting to major modifications of the plant.

The paper is organized as follows: the use of MEMS inertial sensors to improve the performance of motion control systems with low-resolution positions sensors is presented in Sect. 2. It will be shown how accuracy and robustness can be improved, compared to standard solutions. As for the improvement of the performance of motion control systems driven by stepper motors, the problem is two-folded. In Sect. 3 it will be shown how it is possible to use load-side MEMS sensors to determine and compensate the principal components of the torque ripple in Hybrid Stepper Motor, which severely limit the performance attainable with this type of actuators. In Sect. 4, we propose the use of an active damping strategy, which allows for the improvement of the dynamic response and an excellent rejection of the oscillations caused by the torque ripple. Section 5 reports some final remarks.

2. Positioning Performance Improvement with MEMS Sensors

In this section, we propose the use of a KF, which implements a sensor fusion, in order to reduce the effects of the quantization noise affecting the measured position. In particular, the KF utilizes the measurements provided by a low cost MEMS accelerometer to enhance the quality of position and velocity estimates, to be used in the closed loop position control of a table system. The size and cost of the additional sensor are negligible, so it can be easily mounted on an existing system, to improve its original performance. The use of load acceleration sensing, combined with a KF, is not new in motion control, but the solution proposed here has some original features, compared to the existing ones. In [7], the measurements provided by the accelerometers is used to get a velocity signal with reduced noise, compared to that obtained by the differentiation of the position provided by an incremental encoder. The robustness of the estimate is also enhanced by making use of a kinematic KF, in place of the usual one, based on the dynamic model of the plant. Another relevant application can be found in the sensorless force control proposed in [8], where the measurement provided by the accelerometer is used in an advanced implementation of the Disturbance Observer (DOB), to obtain a better estimate and compensation of the disturbances. In both cases, however, authors do not explicitly take into account the issue of bias affecting the acceleration measurements. IAdditionally, the results reported do not consider the scenario of a servo positioning device, limiting the discussion to velocity or force control. As mentioned above, we are interested in the possibility of improving the performance of an existing servo positioning system, equipped with a low resolution position sensor. In this section, we present a solution based on an acceleration-based disturbance observer (a-DOB). In this implementation of the disturbance observers, an augmented model of the acceleration measurement is used to take into account bias and drifts in the measurements provided by the MEMS sensor. Similarly to the solution proposed in [7], the Kalman filter is based on a kinematic model, and the estimates are used not only to determine the disturbance acting on the system as in [8], but also to get a smooth and large bandwidth estimate of load position and velocity.

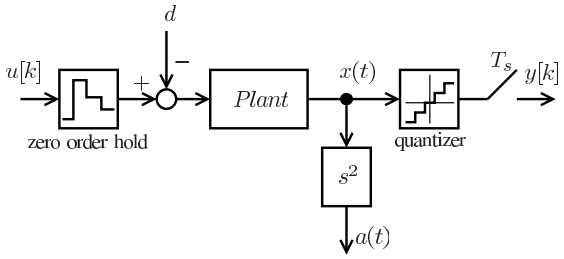

Fig. 1. Block diagram of the plant model

2.1 Kalman Estimator Utilizing a MEMS Accelerometer

In this subsection, we develop the model and the Kalman estimator for a rigid, single degree of freedom servo positioning system, composed of a linear motor on which a position sensor and a MEMS accelerometer provide the load mass position and acceleration, respectively. When considering the force as the system input and the position as output, the plant block diagram results as in Fig. 1, where u is the force command provided by the controller, d the input disturbance force, a is the actual acceleration of the load and x and $\dot{x}$ are the load position and velocity, respectively (so that $a = \ddot{x}$). For such a system, it is possible to design a kinematic state estimator, which makes use of the measured acceleration and load position to obtain a smooth and robust estimate of the system states, as proposed in [7]. The robustness is ensured by the fact that, by knowing the actual load acceleration and considering it as the system input, the load mass is no longer included in the system dynamics, thus ensuring an accurate estimate even in case of large variations of the actual load mass. In [7], it is assumed that the acceleration measurement is accurate and bias free. This, however, is not true, especially when acceleration measurement is made by using low cost MEMS accelerometers. In general, The presence of bias is particularly detrimental in all those applications where the acceleration signal is used to obtain the velocity and/or position of a device on which the sensor is mounted. This is the typical scenario of inertial navigation, in which the coordinates and velocities of a vehicle (terrestrial or aerial) are obtained by integrating the measurements of a set of inertial sensors (e.g. accelerometers and gyroscopes). On the other hand, Global Positioning Systems provide drift-free measurements, but at a low sampling rate and with an unsatisfactory degree of accuracy. To achieve the desired goal of accurate, drift-free and frequent estimate of the position (and/or velocity), several so-called *sensor fusion* techniques have been developed, in which the positive characteristics of the GPS sensor are blended with those of the inertial one. Interested readers can deepen the subject in [9] and [10]. In a nutshell, most of the techniques for the cancellation of the bias are based an integrator, which accumulates the difference between the GPS position and that obtained by the double integration of the accelerometer's output. This initial approach has been further developed in a state-space, stochastic framework, where errors, noise and bias are all treated as random processes. Additionally, the research on MEMS sensors has

shown that the errors in their measurements are a combination of random error sources, non linearities and thermally induced alterations. A global analysis on the model of errors in MEMS accelerometers can be found in [11], while a more detailed modeling of their measurement noise is reported in [12], where the use of Allan's variance is clearly described. Finally, a comprehensive analysis on the bias in the measurements has been conducted in [13]. Here, it can be seen that the bias has by far a more complex description than a stochastic process, being related also to operating temperature. Of course, many of the above-mentioned issues can be partially or totally solved by implementing an accurate calibration of the sensors (to determine scale factors and bias) and implementing a strict temperature control (or compensation). In the mechatronic application analyzed in this paper, however, this would require a specific calibration of each sensor after placement on the servo positioner to be controlled, increasing the implementation cost. In order to address all the above issue at a reasonable implementation cost, it is proposed here to make use of a simplified model of the acceleration measurement (compared to that proposed in [11]), which considers the actual acceleration a as the sum of the measured one plus a bias and a noise, i.e.

$$a = a_m + a_b + w_1 \cdots\cdots (1)$$

where a_m represent the measurement of the load acceleration, as provided by an accelerometer, a_b is the bias and noise w_1. The measurement bias is modeled as a random walk, i.e.

$$\dot{a}_b = w_2 \cdots\cdots (2)$$

with w_2 a white random process.

It is worth noticing that the proposed model, far from being complete, is however capable of capturing several important characteristics of the MEMS sensor, namely the wide-band noise, the bias and its possible variations, including those induced by the operating temperature and the changes in the scale factor.

Going back to [7], it is proposed in this paper to extend such approach, by embedding the above model for the biased acceleration measurement into the kinematic model of the servo positioner, resulting in the following space state model, describing the dynamics between the acceleration measurement a_m and the measured position y:

$$\dot{x} = Ax + B_1 a_m + B_2 w \cdots\cdots (3)$$
$$y = Cx + v \cdots\cdots (4)$$

where $x = [x,\ \dot{x},\ a_b]^T$, $w = [w_1,\ w_2]^T$ and

$$A = \begin{bmatrix} 0 & 1 & 0 \\ 0 & 0 & -1 \\ 0 & 0 & 0 \end{bmatrix},\ B_1 = \begin{bmatrix} 0 \\ 1 \\ 0 \end{bmatrix},\ B_2 = \begin{bmatrix} 0 & 0 \\ -1 & 0 \\ 0 & 1 \end{bmatrix},$$
$$C = \begin{bmatrix} 1 & 0 & 0 \end{bmatrix} \cdots\cdots (5)$$

The process noises w_1, w_2 and measurement noise v are white Gaussian random processes with zero mean and variances σ_a^2, σ_b^2 and σ_R^2, respectively, and they account for different noise and error sources, including the accelerometer output noise, the quantization of the position encoder, and other modeling errors.

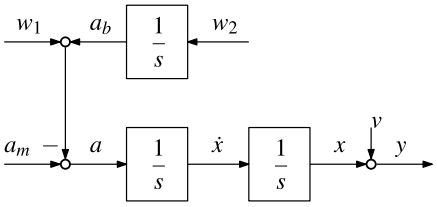

Fig. 2. Block diagram of the continuous time plant model used for the Kalman filter design

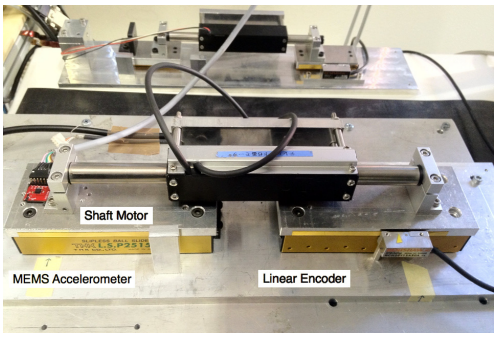

Fig. 3. Picture of the experimental setup

The block diagram of the continuous time model (3), (4), used for the design of the kinematic KF, is reported in Fig. 2. Its zero-order hold discretization has been used for the design of a time-varying KF, in which the variance of the measurement noise is $\sigma_R^2 = q^2/12$, with q being the position sensor resolution (quantization step). On the other hand, the determination of the process noise variances is not so immediate. Process input noise variance σ_a^2 can be obtained experimentally, by performing an Allan's variance test on the data obtained using a steady MEMS accelerometer or using data provided by the manufacturer. As for the, variance of w_2, this must determined experimentally, by performing a whiteness test (e.g. Bartlett's test [14]) on the process innovation, i.e. the value of σ_b^2 is varied until difference between the actual and the estimated system outputs, during the actual motion of the servo positioner, gets as close as possible to a white noise. In fact, it is not possible to use data from the Allan's variance test, due to simplicity of the model for the bias used here, for which variations in scale factor due to nonlinearity or variations of bias due to temperature (both not accounted in Allan's variance) will result in variations of the estimated measurement bias. Anyway, this experimental tuning usually leads to satisfactory results, even if not optimal in a stochastic sense. As a final remark, it is worth noticing that the KF estimator used here can be seen an extension to the stochastic case of the Unaccessible Input Observer proposed in [15], where the unaccessible input is the bias of the MEMS accelerometer in the system considered. In particular, approach followed in this paper is inspired to the research on the zero-order model for the bias reported in [16] and later extended to the stochastic case in [17].

2.2 Experimental Setup Figure 3 shows the experimental setup used to test the use of Kalman filter in the control of the position with low resolution encoders. It is composed of a linear shaft brushless motor, moving a mechanical load consisting of two slides, mounted on two linear ball bearings guides.

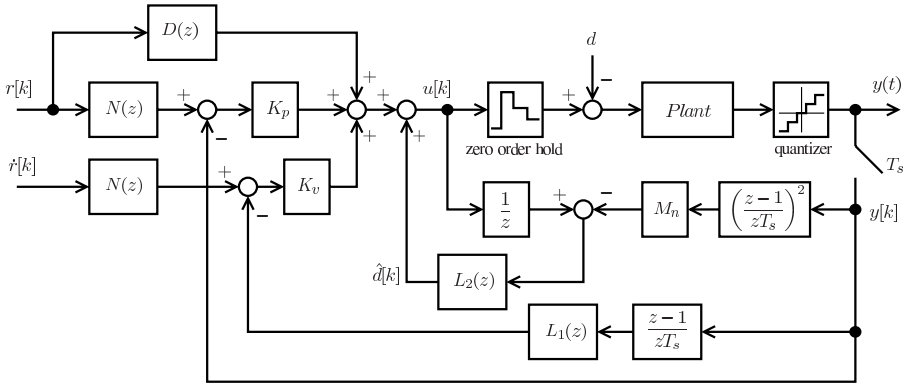

Fig. 4. Block diagram of conventional control system consisting of p-DOB with PD regulator based on measured position information (conventional)

Table 1. Specifications of experimental setup

continuous force	20	N
peak force	78	N
magnetic pitch (North-North)	60	mm
length	80	mm
linear sensor resolution	10	μm
sampling time T_s	500	μs
load mass M	2	kg

Table 2. Controller parameters of conventional system

proportional gain	K_p	[N/m]	7900
differential gain	K_v	[N/(m/s)]	250
cut off frequency of $N(s)$ and $D(s)$	ω_f	[rad/s]	100π
cut off frequency of $L_1(s)$	ω_{l1}	[rad/s]	200π
cut off frequency of $L_2(s)$	ω_{l2}	[rad/s]	60π
sampling time	T_s	[ms]	0.5

The position of the load is measured by a linear encoder with 10 μm resolution. A low cost MEMS accelerometer (Analog Devices' ADXL335 3-Axis accelerometer [18]) is placed on top of one slide, to measure its acceleration. The linear motor is driven by a servo amplifier, which receives the thrust force command given by the control system. This is computed with sampling time T_s on Matlab/Simulink with Real-Time Windows Target. The specifications of the system are listed in Table 1.

2.3 2-degrees-of-freedom Control System In order to test the effectiveness of the proposed solution, a fair comparison of the control performance achievable with different solutions had to be made. In the following we will present two alternative position servo controllers for the experimental system described in Sect. 2.2.

Both of them implement a robust 2-degrees-of-freedom (2DOF) PD controller, designed by using a slightly modified version of the solution presented in [19], where a robust PI controller was designed for a velocity servo.

2.3.1 Conventional: p-DOB with PD Regulator based on Measured Position Information The first controller is reported in Fig. 4, which shows a 2DOF positioning system, consisting of p-DOB with PD regulator based on measured position information, where $N(z)$ and $D(z)$ are feedforward compensators, K_p is a position gain, K_v is a velocity gain, M_n is a nominal weight of the table, $L_1(z)$ is a first order low pass filter, $L_2(z)$ is a second order low pass filter, $r[k]$ is a position reference, $\dot{r}[k]$ is a velocity reference, $u[k]$ is a thrust force command, $y(t)$ is a table position, $y[k]$ is a measured table position, d is a disturbance and $\hat{d}$ is an estimated disturbance.

As mentioned above, all the discrete-time filters and controllers are the discrete versions of continuous-time counterparts. In particular, the first order low pass filter $L_1(s)$ has been designed for filtering of the discrete-time differentiation of the measured position, with the following transfer function:

$$L_1(s) = \frac{\omega_{l1}}{s + \omega_{l1}} \cdots\cdots (6)$$

The second order low pass filter $L_2(s)$ has been designed with narrower bandwidth compared to $L_1(s)$ (cut off frequency of 30 Hz), in order to reduce the noise due to the double differentiations of the quantized measured position.

$$L_2(s) = \frac{\omega_{l2}^2}{(s + \omega_{l2})^2} \cdots\cdots (7)$$

The feedforward compensators have been designed, according to the coprime factorization of the rigid model $P_M(s) = 1/(M_n s^2)$; it holds that:

$$N(s) = \frac{\omega_f^2}{(s + \omega_f)^2}, \qquad D(s) = \frac{M_n \omega_f^2 s^2}{(s + \omega_f)^2} \cdots\cdots (8)$$

Finally, the feedback controller is a standard proportional-derivative (PD) regulator with transfer function

$$C(s) = K_p + K_v \cdot s, \cdots\cdots (9)$$

where the controller parameters are listed in Table 2.

2.3.2 Proposed Solution: a-DOB with PD Regulator based on Estimated Position Information Figure 5 shows the 2DOF positioning system consisting of a-DOB with PD regulator based on estimated position. Again, the design of the controllers and filters is the same as above, with the main difference in the use of the Kalman filter in order to estimate of the whole system state, which includes the acceleration bias $\hat{a}_b[k]$, in addition to $\hat{x}[k]$ (estimated position) and $\hat{\dot{x}}[k]$ (estimated velocity). With this solution, the accuracy and the speed of the disturbance estimate no longer depends on the noise and/or the quantization affecting the position measurement. For this reason, it is possible to widen the bandwidth of the low-pass filter on the estimated disturbance, resulting in the set of parameters reported in Table 3.

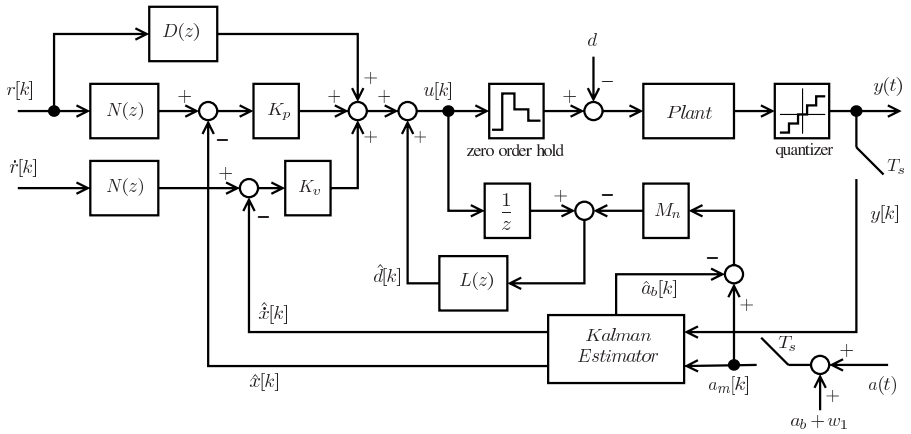

Fig. 5. Block diagram of the proposed control system consisting of a-DOB with PD regulator based on estimated position information (proposed)

Table 3. controller parameters of proposed system

proportional gain	K_p	[N/m]	7900
differential gain	K_v	[N/(m/s)]	250
cut off frequency of $N(s)$ and $D(s)$	ω_f	[rad/s]	100π
cut off frequency of $L(s)$	ω_l	[rad/s]	80π
sampling time	T_s	[ms]	0.5

2.4 Experimental Verifications In order to verify the positioning performance of the proposed system, a S-shaped position reference with amplitude of 70 mm and travel time of 0.5 s is applied to the system. The performance of the conventional position based disturbance observer (p-DOB) is compared with that obtained with the proposed a-DOB, described in the previous section. It is worth noticing that in the p-DOB the load acceleration (required for the estimation of the input disturbance) has been obtained by filtering the load position measurement with a second order high-pass filter. As mentioned in the previous section, a cut-off frequency of 60 Hz has been chosen to get a satisfactory reduction of the high frequency noise caused by the double differentiation of the low-resolution position measurement. This results is a slow response of the overall system, compared to the proposed solution, which does not implement such filtering. Figures 6 and 8 show response waveforms of (a) table position, (b) thrust force command and (c) acceleration measured by a MEMS accelerometer without and with load conditions, respectively. Figures 7 and 9 are magnified plots of position responses for positive and negative motions. Positioning performances under load conditions are clearly deteriorated by the additional weight, in comparison to no-load performances. The estimation bandwidth of the p-DOB cannot be easily increased, due to the presence of the noise caused by the differentiation of the low resolution position signal. Its effect can be noticed in some high frequency vibration, occurring before settling at the target position. As for the proposed control system, based on a-DOB, it achieves a better positioning performance. As it can be seen in the experimental results reported in Figs. 10 to 13, the proposed method achieves the shortest rise time and the best rejection of the effects of the load mass variation. Settling is faster, compared to the other method.

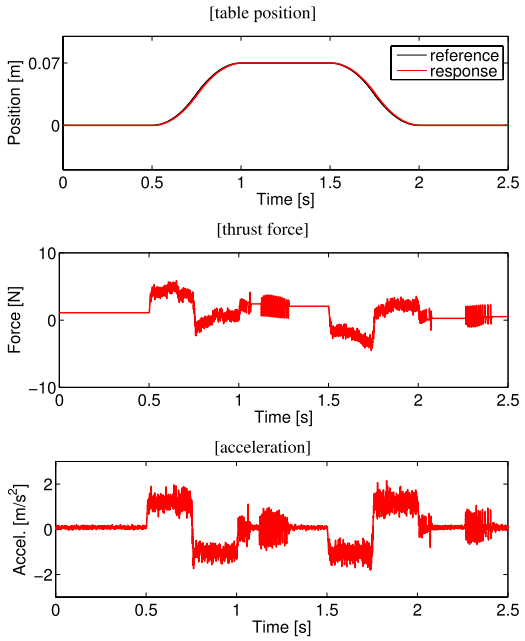

Fig. 6. Response waveforms for S-shaped position reference of conventional control system consisting of p-DOB with PD regulator based on measured position information without additional load weight ($M = M_n$)

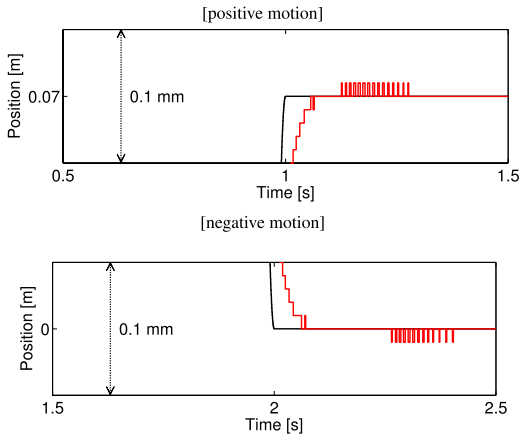

Fig. 7. Magnified position waveforms of Fig. 6

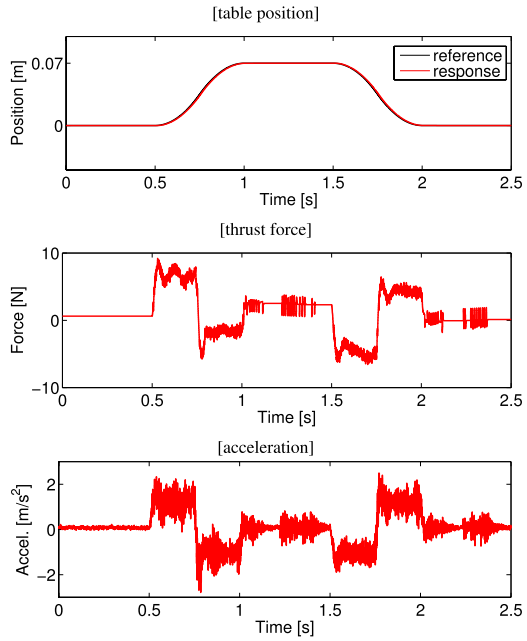

Fig. 8. Response waveforms for S-shaped position reference of conventional control system consisting of p-DOB with PD regulator based on measured position information with load weight ($M = 2M_n$)

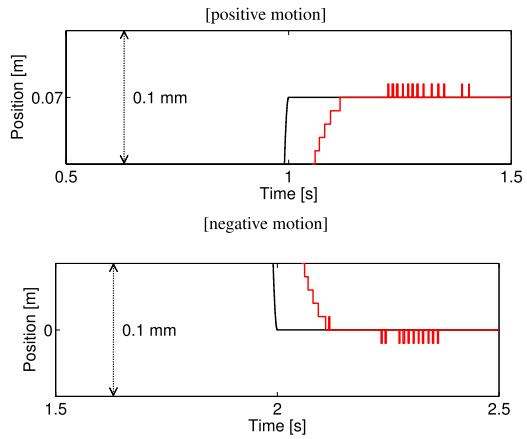

Fig. 9. Magnified position waveforms of Fig. 8

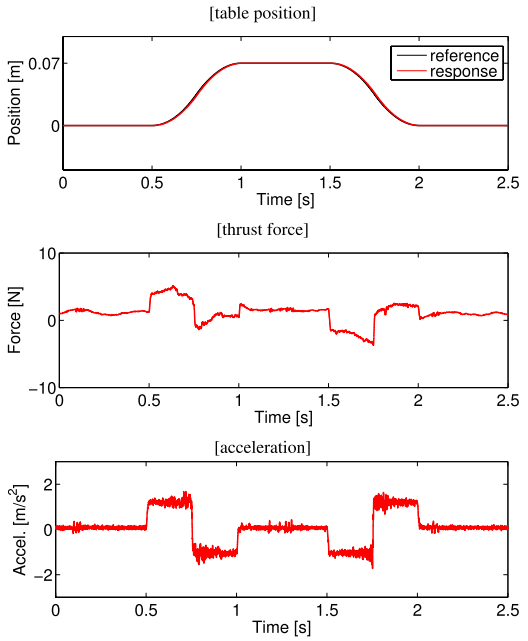

Fig. 10. Response waveforms for S-shaped position reference of proposed control system, consisting of a-DOB with PD regulator based on estimated position information without additional load weight ($M = M_n$)

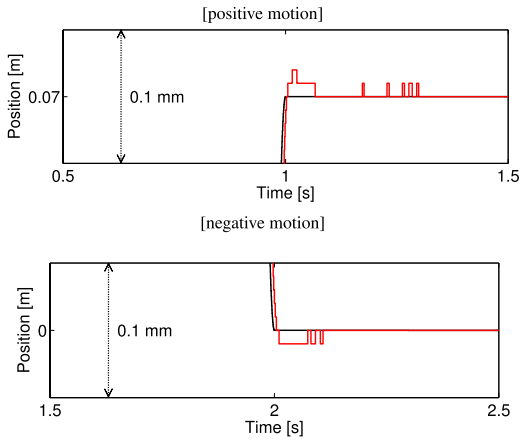

Fig. 11. Magnified position waveforms of Fig. 10

3. Ripple Torque Minimization in HSM

Stepper motors are commonly used in those motion control applications that do not require extremely high positioning accuracy, but instead impose constraints on cost and complexity of the driving circuits. Hybrid stepper motors (HSMs) are a particular kind of stepper motors, combining the operating principles of the variable reluctance (VR) and permanent magnet (PM) motors [20]. As matter of fact, the torque generated by HSMs is affected by undesired pulsations (harmonic components) that produce an irregular motion of the load. Such non-smoothness of the torque becomes rather problematic in case of a resonant load. In such a case, in fact, the torque ripple could excite the load resonances, thus inducing large oscillations. Given the previous considerations, the reduction of torque ripple is highly desirable in HSM-driven motion control applications. A common practice to address this issue is the use of a sine-cosine microstepping excitation scheme, in which the two stator phases are excited with two sinusoidal quadrature currents. However, as shown later, this solution, cannot definitely remove the torque ripple.

3.1 HSM Torque Ripple

In the following, we derive the analytical expression of the torque in a HSM by applying the principle of energy conservation; we will assume that no magnetic saturation occurs in the magnetic circuit (i.e. the magnetic flux is proportional to the stator currents and independent of the internal magnet). At first, it can be proved [21] that the motor torque τ_m, w.r.t. the rotor position θ, is equal to

$$\tau_m = \frac{1}{2} i^T \frac{\partial L}{\partial \theta} i \quad \cdots\cdots (10)$$

where L is a 3×3 symmetric positive definite inductance matrix

$$L = \begin{pmatrix} L_{11} & L_{12} & L_{1f} \\ L_{12} & L_{22} & L_{2f} \\ L_{1f} & L_{2f} & L_{ff} \end{pmatrix} \quad \cdots\cdots (11)$$

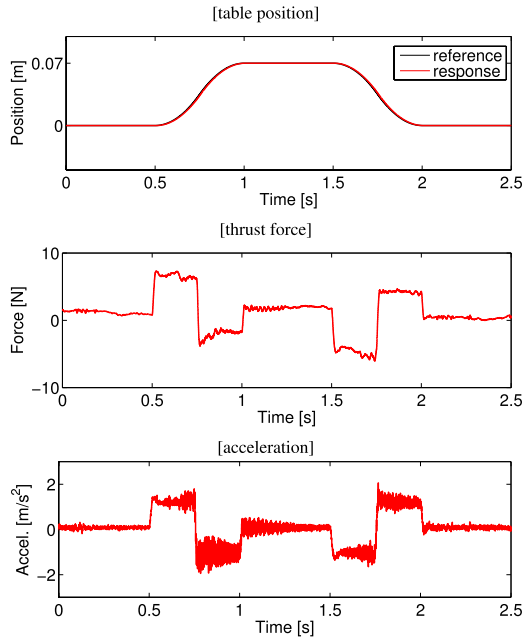

Fig. 12. Response waveforms for S-shaped position reference of proposed control system, consisting of a-DOB with PD regulator based on estimated position information with load weight ($M = 2M_n$)

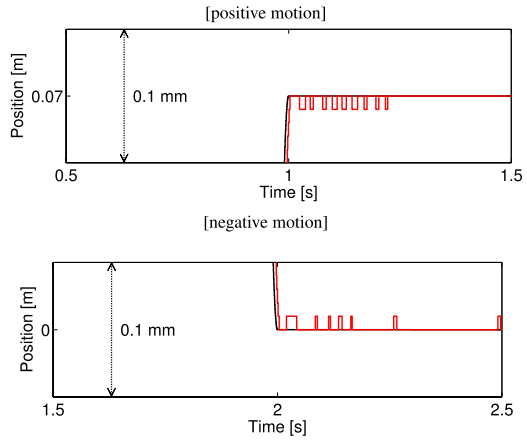

Fig. 13. Magnified position waveforms of Fig. 12

and $i = [i_1, i_2, i_f]^T$, with i_1, i_2 the the winding currents in, respectively, phase 1 and phase 2, and i_f is the constant fictitious field current, responsible for the magnetic field produced by the permanent magnet. In the inductance matrix, L_{11} and L_{22} are the self-inductances of windings 1 and 2, L_{12} is the mutual inductance between the two windings, L_{1f} and L_{2f} are the mutual inductances between the two windings and the fictitious rotor winding, and L_{ff} is the self-inductance of the fictitious rotor winding. The torque expression 10 can be expanded as follows

$$\tau_m = \tau_{pm} + \tau_{vr} + \tau_{cg} = \left(\frac{\partial L_{1f}}{\partial\theta} i_1 i_f + \frac{\partial L_{2f}}{\partial\theta} i_2 i_f\right) + \left(\frac{1}{2}\frac{\partial L_{11}}{\partial\theta} i_1^2 + \frac{1}{2}\frac{\partial L_{22}}{\partial\theta} i_2^2 + \frac{\partial L_{12}}{\partial\theta} i_1 i_2\right) + \frac{1}{2}\frac{\partial L_{ff}}{\partial\theta} i_f^2 \quad \cdots\cdots\cdots\cdots\cdots\cdots (12)$$

The first term in round brackets is the torque component generated by the interaction of the magnetic fields of the stator windings and the permanent magnet. The second term is the *reluctance torque*, which depends on the variations in self and mutual inductance of the windings (mainly due to geometric imperfections and rotor anisotropy). The last term is usually refers as the *cogging* (or *detent*) *torque*, mainly due to variations in self-inductance of the fictitious rotor winding, caused by the presence of slots in the stator (minimum reluctance path). It is worth noticing that the cogging torque is present even in absence of winding currents; its periodicity with respect to the rotor position is equal to the periodicity at which the slots are located along the stator.

All the entries of the inductance matrix are periodic functions of the rotor position θ, and their basic frequencies can be deduced from the symmetries of the motor. Denoting with N_r the number of rotor teeth, it holds that

$$\begin{aligned} L_{11}(\theta) &= L_0 + L_1\cos(2N_r\theta) \cdots\cdots\cdots\cdots\cdots\cdots (13)\\ L_{22}(\theta) &= L_0 - L_1\cos(2N_r\theta)\\ L_{12}(\theta) &= -\frac{L_0}{2} + L_1\sin(2N_r\theta)\\ L_{1f}(\theta) &= L_{m0} + \sum_{j=1}^{n} L_{mj}\cos(jN_r\theta)\\ L_{2f}(\theta) &= L_{m0} + \sum_{j=1}^{n} L_{mj}\sin(jN_r\theta)\\ L_{ff}(\theta) &= L_{f0} + \sum_{j=4}^{n} L_{fj}\cos(jN_r\theta) \cdots\cdots\cdots\cdots\cdots (14) \end{aligned}$$

where n is the number of harmonics considered in the expression of the motor torque. Higher order harmonics ($n \geq 2$) in the mutual inductance terms L_{1f} and L_{2f} model the nonsinusoidal (with respect to the rotor angle) flux distribution in the airgap.

In a typical (ideal) hybrid stepper motor, the variation of phase inductance is as small as a few percent, and its contribution to the total torque is negligible; moreover, the surfaces of the rotor and stator teeth are usually shaped in such a way that the magnetic flux in the airgap is fairly sinusoidal. By setting

$$L_{11} = L_{22} = L_0, \quad L_{12} = 0, \quad L_{mj} = 0 \quad j \geq 2 \cdots\cdots (15)$$

in the self and mutual inductances (13)–(14), and replacing them in the torque components, (12) yields

$$\begin{aligned} \tau_{pm} &= -i_1 i_f L_{m1} N_r \sin(N_r\theta) + i_2 i_f L_{m1} N_r \cos(N_r\theta)\\ \tau_{cg} &= -\frac{1}{2}\sum_{j=4}^{n} L_{fj} jN_r \sin(jN_r\theta) i_f^2 \cdots\cdots\cdots\cdots\cdots (16) \end{aligned}$$

and $\tau_{vr} = 0$.

As mentioned before, a standard approach used to generate a constant torque is to use a microstepping driving technique, in which two sinusoidal quadrature currents are applied to the stator windings:

$$i_1 = I\cos(N_r\theta_u), \quad i_2 = I\sin(N_r\theta_u) \cdots\cdots\cdots\cdots (17)$$

where θ_u is the angular position of the stator flux. In fact, replacing (17) in (16) yields:

$$\tau_{pm} = i_f L_{m1} N_r I \sin[N_r(\theta_u - \theta)] \cdots\cdots\cdots\cdots (18)$$

Hence, the torque τ_{pm} is constant whenever the angle $\rho = \theta_u - \theta$, called *torque* (or *load*) *angle*, is constant.

In practice, due to unbalancing and imperfections of the driving amplifiers, the phase currents will always be affected by some offset, and their amplitude will be unmatched. By taking into account the offsets and gain unbalancing in the expressions of phase currents, i.e.

$$i_1 = I_{10} + I_{11}\cos(N_r\theta_u), \quad i_2 = I_{20} + I_{21}\sin(N_r\theta_u) \qquad \cdots\cdots\cdots\cdots\cdots (19)$$

and replacing them in 16 yields:

$$\begin{aligned}\tau_{pm} = i_f L_{m1} N_r \Big\{ & \frac{1}{2}(I_{11} + I_{21})\sin[N_r(\theta_u - \theta)] \\ & - I_{10}\sin(N_r\theta) + I_{20}\cos(N_r\theta) \\ & - \frac{1}{2}(I_{11} - I_{21})\sin[N_r(\theta + \theta_u)]\Big\} \cdots\cdots\cdots (20)\end{aligned}$$

For a constant torque angle $\rho = \theta_u - \theta$, two harmonic components show up in the torque τ_{pm}, in addition to a constant term. The first harmonic component of the torque ripple in τ_{pm} has the same frequency of the phase currents and an amplitude depending on the current offsets I_{10} and I_{20}; the second component has twice the frequency of the phase currents and an amplitude depending on the unbalancing of the phase current amplitudes I_{11} and I_{21}. This fact will be exploited later in the section to introduce a partial cancellation of the first and second harmonic in the torque ripple.

3.2 Torque Ripple Minimization in HSMs Torque ripple reduction or compensation in permanent magnet synchronous motors has been widely studied and a rather complete review on various methods is reported in [22]. Such methods can be broadly classified in two major groups: 1) methods based on the improvement of the motor design, and 2) methods based on the improvement of the stator current driving, possibly taking advantage of feedforward or closed control loop schemes, in order to compensate the unideal characteristics of the motor.

Differently from the majority of the solutions found in literature, the procedure for torque ripple reduction proposed in this paper does not require neither expensive high-resolution encoder for measuring the rotor angular position nor modifications of the magnetic structure of the motor; instead, it exploits a low-cost MEMS accelerometer to detect the vibration induced by the torque ripple on the load-side. As it will be show later, another advantage of the proposed solution is that it can be easily fitted in existing equipments, without major interventions.

The proposed procedure, reported in detail in [23], is conceived to minimize the torque ripple contribution induced by imperfections in the generation of the current profiles when using a microstepping excitation scheme. The compensation scheme is based on the observation that, under the assumption made in Sect. 3.1, the nonzero current offsets produce a torque harmonic disturbance component at the same frequency of the driving currents, while the amplitude unbalancing between the two current phases generates a second harmonic at twice the frequency of the driving currents.

With reference to 20, it can be noted that the two torque ripple harmonics have magnitudes

$$\begin{aligned}|\tau_{pm,1}| &= i_f L_{m1} N_r \sqrt{I_{10}^2 + I_{20}^2} \\ |\tau_{pm,2}| &= i_f L_{m1} N_r \frac{1}{4}|I_{11} - I_{21}| \cdots\cdots\cdots\cdots\cdots (21)\end{aligned}$$

i.e. the squared magnitude of the first harmonic depends quadratically on the current offsets I_{10} and I_{20}, while the squared magnitude of the second harmonic depends quadratically on the amplitude unbalancing $I_{11} - I_{21}$. This observation allows to formulate a multi-step minimization procedure, in which some current offsets and gain unbalancing are deliberately introduced in the phase currents, and then varied to seek for a minimum of the amplitude of the first two harmonics of the acceleration ripple measured by the MEMS accelerometer.

The procedure can be summarized in the following steps:

(1) do a first experiment in which the ideal microstepping excitation scheme (19) is modified as follows
$i_1 = \hat{I}_{10} + I\cos(N_r\theta_u), \quad i_2 = I\sin(N_r\theta_u)$
where the offset $\hat{I}_{10}$ is slowly varied over a specified range (fraction of the rated current I), while the rotor moves with almost constant velocity (i.e. while θ_u is slowly linearly increased), until the optimal offset compensation value $\hat{I}_{10}^*$, minimizing the first harmonic of the torque ripple is found.

(2) do a second experiment in which the previous step is repeated for the second phase current. Use the modified microstepping excitation scheme
$$i_1 = \hat{I}_{10}^* + I\cos(N_r\theta_u), \; i_2 = \hat{I}_{20} + I\sin(N_r\theta_u)$$
where the offset $\hat{I}_{20}$ is slowly varied over a specified range. Obtain the optimal offset compensation value $\hat{I}_{20}^*$ by repeating the procedure described in the previous step.

(3) do a third experiment in which the ideal microstepping excitation scheme (19) is modified as follows
$$i_1 = \hat{I}_{10}^* + \hat{I}_{11}\cos(N_r\theta_u), \; i_2 = \hat{I}_{20}^* + \hat{I}_{21}\sin(N_r\theta_u)$$
where $\hat{I}_{11}$ is slowly varied over a specified range (across the rated current I), while $\hat{I}_{21} = 2I - \hat{I}_{11}$. The last condition guarantees that the average torque provided to the load is kept constant. The minimum value of the second harmonic of the torque ripple is achieved with the optimal amplitude value $\hat{I}_{11}^*$ for the phase current i_1 (and, indirectly, the optimal amplitude value $\hat{I}_{21}^*$ for the phase current i_2).

3.3 Experimental Results The proposed procedure for minimizing the torque ripple in hybrid stepper motors has been tested on a commercial bipolar, two-phase HSM with 1.8° step angle (50 rotor teeth), used for generating the pan motion in a positioning unit for surveillance cameras (see Fig. 14).

A MEMS linear accelerometer has been placed on top of the camera, as shown in Fig. 15, to measure the tangential acceleration of the unit; then, the angular acceleration can be derived by measuring the distance of the accelerometer from the rotation axis. Clearly, no major modifications on the existing hardware have been made and only the wiring between

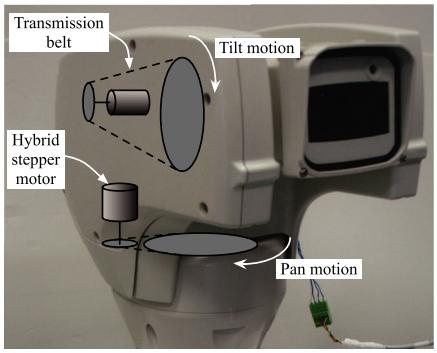

Fig. 14. Positioning unit for surveillance cameras

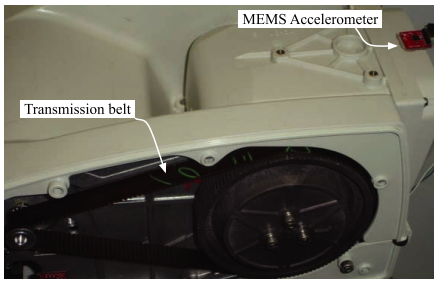

Fig. 15. MEMS accelerometer placement on top of the camera case

the sensor and the control unit is added.

Two sinusoidal phase currents with a nominal amplitude of $I = 1$ A and a frequency of 20 Hz (corresponding to an angular velocity of $\approx 21°$/s for the pan motion) have been used in the experiments. The driving frequency has been chosen in order not to excite the mechanical resonances, described in the next section. In such a way, a more regular motion is produced and the effects produced by varying the current offsets/amplitudes can be highlighted more clearly. In performing the experiments, we purposely skipped the initial calibration of the offsets and gains of the linear amplifiers used to drive the two motor phases, so the phase currents were affected by some offset and gain unbalancing. The application of the procedure described in the previous section yields the results collectively reported in Fig. 16. The minimization of the first harmonic amplitude has been achieved with the offset values $\hat{I}^*_{10} = -0.121$ A and $\hat{I}^*_{20} = -0.055$ A (see the top plots of Fig. 16). The minimization of the second harmonic amplitude is obtained with the amplitude values $\hat{I}^*_{11} = 0.847$ A and $\hat{I}^*_{21} = 2\,I - \hat{I}^*_{11} = 1.153$ A.

It is worth noticing that the measured square magnitudes of the first two acceleration harmonics depend quadratically on the two current offsets and the amplitude unbalancing, thus legitimating the assumptions made in Sect. 3.1 for deriving the torque expression (20).

The benefits of the proposed compensation procedure in minimizing the first two harmonics of the torque ripple can be also appreciated in the acceleration spectrum measurements reported in Fig. 17. The compensation of the current offsets drastically reduces the amplitude of the first harmonic (at 20 Hz); the minimization of the second harmonic amplitude is less evident (at 40 Hz), perhaps due to the fact that the initial gains of the driving amplifiers were almost balanced before applying the compensation procedure. It is worth

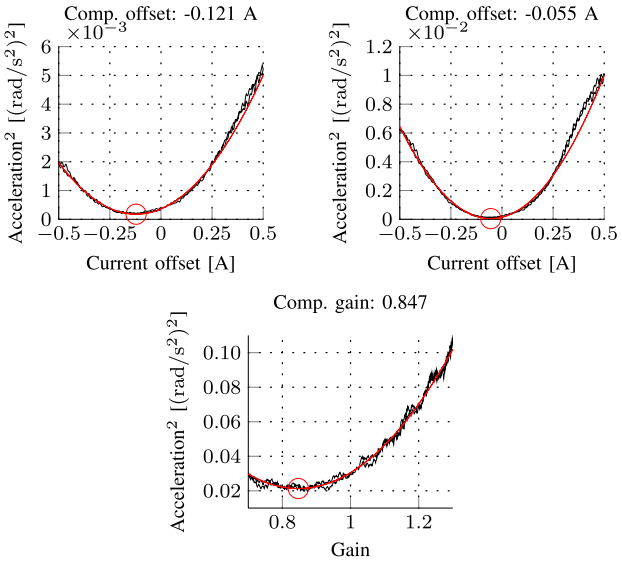

Fig. 16. Determination of the optimal phase current offsets (top plots) and amplitude unbalancing (bottom plot)

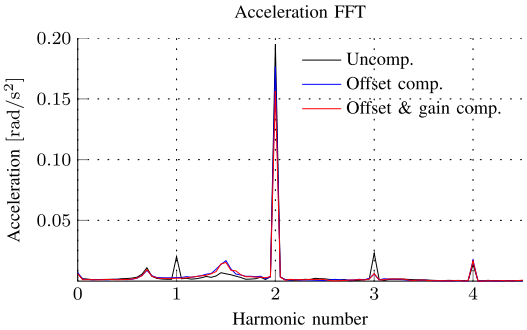

Fig. 17. Acceleration ripple (load-side) spectrum before and after the compensation procedure

noticing that the use MEMS accelerometers usually brings in some problems, due to bias in the measurements as well as inaccuracy in the scale factor. The proposed method, however, is insensitive to bias on acceleration measurement, given that the analysis on the spectrum is performed at non-zero ripple frequency. As for the scale factor, it does not affect the effectiveness of the proposed procedure, as the latter searches for the minimum of the measured acceleration due to the first two harmonics of the ripple torque (21), which has a convex relation with the tunable parameters.

4. Active Vibration Damping in HSM-Driven Mechanical Systems with Elesticity

In the previous section, we have presented a solution for reducing the torque ripple generated by a HSM, by properly tuning the gains and the offsets of the phase current amplifiers. It can be noticed, however, that the cancellation is not complete and higher order harmonics cannot be reduced. As described in literature, the complete cancellation of torque ripple requires the injection of compensation stator currents that should change according to the absolute position of the rotor. This, however, would require a rotor position sensor and, in turn, a major hardware modification. With a residual ripple torque it is still possible to experience severe limitations, especially when the HSM is connected to

the mechanical load through an elastic transmission. In this case, in fact, the response of the mechanical system exhibits a resonance, which may amplify the effects of the torque ripple, with large vibrations of the mechanical load and possible pull-out of the HSM. In order to test the feasibility of an active vibration suppression scheme, when the load is driven by a HSM, we used the pan-tilt camera positioning unit described in the previous section, which has an elastic transmission system, in which a pair of reduction gears (reduction ratio $N_G = 1/7$) are connected by a toothed belt. The tracking of a moving target is performed simply by acting on the HSM position, without any feedback, since the unit does not mount a camera position sensor. Rotations of the unit at a constant angular rate ω_t (e.g. when tracking a far target, moving at a constant speed) are obtained with a microstepping drive, with two stator sinusoidal currents in mutual quadrature and with a fixed frequency $\omega_u = (N_r/N_G)\,\omega_t$, where N_r is the number of pole pairs of the HSM and N_G is the gear ratio. In such operating conditions, it may happen that the required rotational speed corresponds to a torque ripple centered on the mechanical resonance of the system and, in this case, the camera may be subjected to large vibrations, making the tracking of the moving target impossible. This phenomenon can be observed in general in HSM-driven motion control systems and it is usually addressed by upper limiting the allowable speed of the system or by allowing only a limited set of fixed motion speeds, not generating torque ripples at the resonance frequencies. In the following we briefly present a solution for the damping of the oscillations induced by the torque ripple and amplified by the mechanical resonance, which does not require a precise dynamic model of the system to be controlled. Further details can be found in [24] and [25].

4.1 Control Design In order to perform the design of the active damping of the vibrational modes for the system described in the previous section, it is vital to derive its dynamic model, relating the control input to the camera position. It is worth noticing that, using the microstepping technique, the stator field can be oriented with an arbitrary angle θ_u, by driving the stator windings with two current in quadrature, namely $i_1 = I\cos(\theta_u)$ and $i_2 = I\sin(\theta_u)$. In absence of a load torque, the rotor aligns its magnetic axis with the stator field (i.e. $\theta_u = \theta_{sh}$). When an external torque τ_m is applied, this causes a displacement between rotor and stator flux, according to

$$\tau_m = K_T\, I\, \sin(\theta_u - \theta_{sh}) \cdots\cdots\cdots\cdots\cdots\cdots\cdots\cdots (22)$$

This, in turn, can be linearized for a small displacement, around the equilibrium, yielding to

$$\tau_m \approx K_T\, I\, (\theta_u - \theta_{sh}) \cdots\cdots\cdots\cdots\cdots\cdots\cdots\cdots (23)$$

Clearly, the above result suggests that the HSM behaves like a spring, with an equivalent stiffness that depends on the motor torque constant K_T and the level of the driving current I.

We identified experimentally the frequency response of the actual system (see Fig. 18). Three different types of connection with the floor are considered, namely with high, medium and zero stiffness K_{base} (the latter obtained by using a ball-bearing support). We can observe that the system shows two evident resonance peaks (which can possibly amplify the torque ripple) at frequencies that clearly depends on the rigidity of the connection.

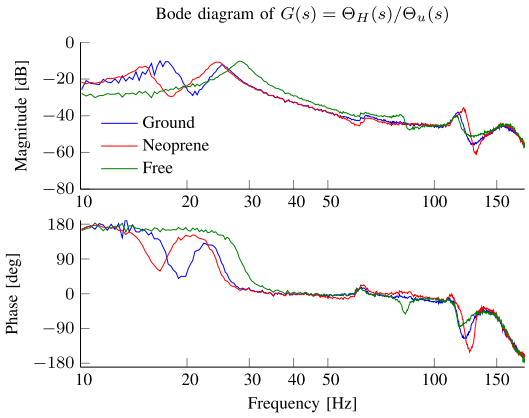

Fig. 18. Experimental frequency response $\Theta_2(s)/\Theta_u(s)$ with different support stiffnesses

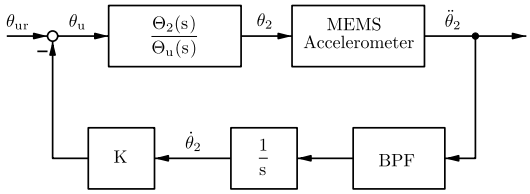

Fig. 19. Active damping inner loop

The rationale behind an active damping strategy is to set up an inner loop, capable of reducing the height of the resonant peaks as well as the oscillations that may be caused by various disturbances. In the following development of such inner control, we must take into account several constraints, due to the use of HSM and to the specific application under study. As for the latter, we must consider that there is no precise knowledge about the transfer function, since it may widely change during operation (e.g. when a bird lands on the camera or the snow piles up un it, the load inertia increases and, in turn, all resonance frequencies decrease). Of course, an online identification procedure could be implemented (e.g. [26]), but this is not compatible with the uninterruptible 24-7 operating scenario of the surveillance camera and the possible sudden and large variations in plant parameters. Then, a typical active damping scheme, with a feedback tuned on the plant resonances (see, for instance, [27]) cannot be applied to the camera positioning unit considered here. Given the above limitation, we resorted to a simple and robust solution, which makes use of a load velocity feedback to generate a torque proportional to the load speed. It can be easily demonstrated that this is equivalent to inserting a viscous damper between load and base.

HSMs, however, are position actuators, so main issue is how to command HSM to generate a damping torque. The solution is provided by (23), which shows that by modulating the stator flux angle θ_u, it is possible to modulate the generated torque as well (this under the hypothesis of small differences between stator and rotor angles). Using the previous consideration, a vibration damping inner loop can be realized in the form shown in Fig. 19, where the load side velocity is obtained by integrating the load acceleration, measured using the MEMS accelerometer. Remarkably, the proposed

method to generate a compensating torque in HSM-driven system can be applied also in systems with fixed plant parameters, for which more sophisticated damping schemes can be applied [27]. In practice, if the target is going to be followed with a constant camera angular speed ω_t, this is achieved by setting the phase currents in the HSM as in (24), (25), where θ_{ur} represents the desired load position:

$$i_1 = I\cos(\theta_{ur}) = I\cos(\omega_{ur}t) = I\cos(N_r/N_G\,\omega_t\,t) \quad \cdots\cdots (24)$$

$$i_2 = I\sin(\theta_{ur}) = I\sin(\omega_{ur}t) = I\sin(N_r/N_G\,\omega_t\,t) \quad \cdots\cdots (25)$$

When the active damping inner loop is active, the actual angular position reference for the stator flux is obtained as follows

$$\theta_u = \theta_{ur} - K\,\dot{\theta}_2 \cdots\cdots (26)$$

i.e. by subtracting a signal proportional to the load angular velocity to the reference angle θ_{ur}. This, as shown above, is equivalent to command the HSM to generate a torque proportional to the load angular velocity, as required by the active damping strategy. Indeed, the design of the inner loop clearly reduces to the choice of the feedback gain K. It is worth noticing that the actual implementation of the inner loop must consider the unavoidable bias and high frequency noise affecting MEMS accelerometer output. Given that the action of the active damping is at the frequency of the mechanical resonance, it is possible to solve the bias and noise issues by filtering the sensor output using a properly tuned band-pass (BP) filter. Doing the filtering before the integration of the acceleration measurement, avoids the presence of both drifts and unwanted noise in the velocity signal $\dot{\theta}_2$. Since the phase quadrature between compensating torque and vibration speed is essential to ensure the damping, the low and high cut frequency of the BP filter are chosen at least one decade lower and one decade higher of the expected resonance frequency, respectively. The resulting control scheme is shown in Fig. 19, in which it can be seen that the strength of the damping action depends on the feedback gain K. As detailed in [25], such gain can be chosen in rather wide range, so making the proposed solution rather insensitive to errors on the scale factor of the MEMS sensor.

4.2 Experimental Results The proposed active damping control has been applied to the camera positioning unit and its effectiveness proven in different operating conditions. Figure 20 shows the comparison of the spectra of the accelerations measured by the MEMS accelerometer, with and without the active damping. The rotating speed is chosen so that the first harmonic of the torque ripple falls in the resonant peak of the frequency response. As a result, a reduction of 95% of the vibration amplitude is achieved.

The same test at constant speed has been performed with different supports (with different rigidity), in order to test the insensitivity of the solution to the mounting conditions. Figure 21 shows the results obtained with teflon and neoprene supports, confirming the robustness of the method.

The robustness against support variations has been tested also in transient conditions (constant acceleration) and the results reported in Fig. 22 confirm the ability of the system to provide an effective damping of all vibratory modes.

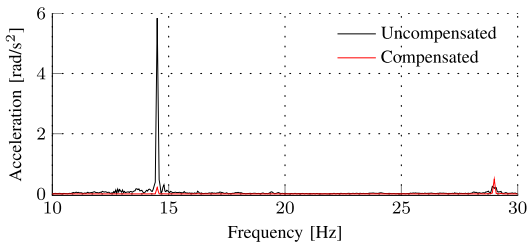

Fig. 20. Vibration attenuation at constant speed

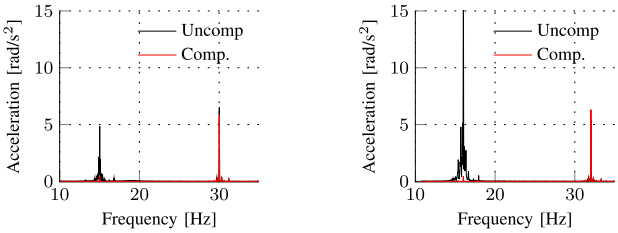

Fig. 21. Vibration attenuation with different supports (teflon on the right, neoprene on the left)—constant speed reference

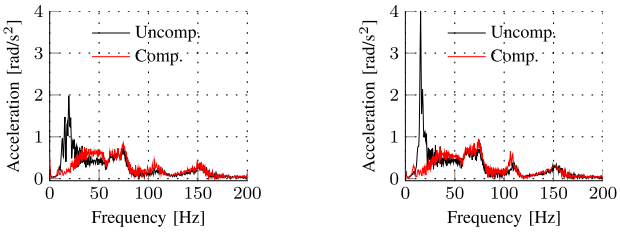

Fig. 22. Vibration attenuation with different supports (teflon on the right, neoprene on the left)—constant acceleration reference

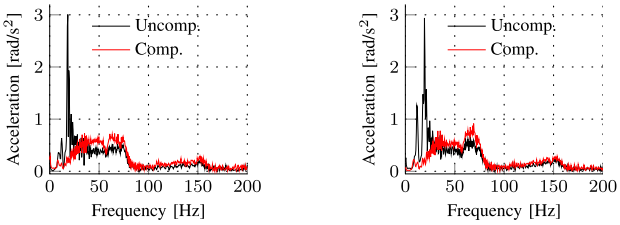

Fig. 23. Vibration attenuation with different load inertia (nominal on the left, doubled on the right)—constant acceleration reference

Finally, the robustness against load inertia variations has been verified, by placing ad additional weight on top of the camera. The results shown in Fig. 23 confirm again the insensitivity of the proposed method to wide changes in operating conditions.

5. Conclusions

In this paper, we have shown how it is possible to largely improve the performance of an existing motion control system, by simply exploiting the measurements provided by low-cost MEMS inertial sensors, mounted on the mechanical load to be controlled. We have shown how it is possible to improve several aspects, ranging from the ripple torque reduction and active damping in HSM-driven systems, to the use of the acceleration measurement in new sensor-fusion schemes, based on the use of Kalman Filters. As a result, the

availability of MEMS inertial sensors open new perspectives in the amelioration of the performance of motion control systems, which can achieve higher performance without major changes in hardware.

References

(1) R.J.E. Merry, M.J.G. van de Molengraft, and M. Steinbuch: "Velocity and acceleration estimation for optical incremental encoders", *Mechatronics*, Vol.20, No.11, pp.20–26 (2010)

(2) M. Nandayapa, C. Mitsantisuk, and K. Ohishi: "High Performance Velocity Estimation for Controllers with Short Processing Time by FPGA", *IEEJ Journal of Industry Applications*, Vol.1, No.1 pp.55–61 (2012)

(3) K. Ohishi, Y. Ogawa, and H. Dohmeki: "Speed Control Method for PM Motor using Speed Observer and Low Resolution Encoder", *T. IEE Japan*, Vol.122, No.3, pp.209–216 (2002) (in Japanese)

(4) R. Kalman and R. Emil: "A New Approach to Linear Filtering and Prediction Problems", *Transactions of the ASME–Journal of Basic Engineering*, Vo.82, No.D, pp.35–45 (1960)

(5) S.-H. Lee, T.A. Lasky, and S.A. Velinsky: "Improved Velocity Estimation for Low-Speed and Transient Regimes Using Low-Resolution Encoders", *IEEE/ASME Transactions on Mechatronics*, Vol.9, No.3, pp.553–560 (2004)

(6) H.-W. Kim and S.-K. Sul: "A New Motor Speed Estimator Using Kalman Filter in Low-Speed Range", *IEEE Trans. Industrial Electronics*, Vol.43, No.4, pp.498–504 (1996)

(7) S. Jeon and M. Tomizuka: "Benefits of Acceleration Measurement in Velocity Estimation and Motion Control", *Control Engineering Practice*, Vol.15, pp.325–332 (2007)

(8) C. Mitsantisuk, K. Ohishi, S. Urushihara, and S. Katsura: "Kalman Filter-Based Disturbance Observer and its Applications to Sensorless Force Control", *Advanced Robotics*, Vol.25, No.3–4, pp.335–353 (2011)

(9) O.J. Woodman: "An introduction to inertial navigation", in Technical Report of University of Cambridge Computer Laboratory, No.696 (2007)

(10) M.S. Grewal, A.P. Andrews, and C.G. Bartone: "Global Navigation Satellite Systems", Inertial Navigation, and Integration, *Wiley-Interscience* (2013)

(11) Park, Minha, and Gao, Yang: "Error and Performance Analysis of MEMS-based Inertial Sensors with a Low-cost GPS Receiver", *Sensors*, Vol.8, No.4, pp.2240–2261 (2008)

(12) A.G. Quinchia, G. Falco, E. Falletti, F. Dovis, and C. Ferrer: "A Comparison between Different Error Modeling of MEMS Applied to GPS/INS Integrated Systems", *Sensors*, Vol.13, No.8, pp.9549–9588 (2013)

(13) F. Gulmammadov: "Analysis, modeling and compensation of bias drift in MEMS inertial sensors", in Recent Advances in Space Technologies, 2009. RAST '09. 4th International Conference on, pp.591–596 (2009)

(14) G.W. Snedecor and W.G. Cochran: Statistical Methods, Iowa State University Press (1989)

(15) J.S. Meditch and G.H. Hostetter: "Observers for systems with unknown and inaccessible inputs", in Decision and Control, IEEE Conference on, pp.120–124 (1973)

(16) B. Friedland: "Treatment of bias in recursive filtering", *Automatic Control, IEEE Transactions on*, Vol.14, No.4, pp.359–367 (1969)

(17) M.B. Ignagni: "Separate bias Kalman estimator with bias state noise", *Automatic Control, IEEE Transactions on*, Vol.35, No.3, pp.338–341 (1990)

(18) http://www.analog.com/en/mems-sensors/mems-inertial-sensors/adxl335/products/product.html

(19) T. Umeno and Y. Hori: "Robust Speed Control of DC Servomotors Using Modern Two Degrees-of-Freedom Controller Design", *IEEE Transactions on Industrial Electronics*, Vol.38, No.5, pp.363–368 (1991)

(20) T. Kenjo: "Stepping Motors and Their Microprocessor Controls", Clarendon Press, Oxford (1984)

(21) F. Khorrami, P. Krishnamurthy, and H. Melkote: Modeling and adaptive nonlinear control of electric motors. Springer-Verlag, Berlin (2003)

(22) T.M. Jahns and W.L. Soong: "Pulsating torque minimization techniques for permanent magnet AC motor drives-a review", *Industrial Electronics, IEEE Transactions on*, Vol.43, No.2, pp.321–330 (1996)

(23) R. Antonello, A. Cenedese, and R. Oboe: "Torque Ripple Minimization in Hybrid Stepper Motors Using Acceleration Measurements", In Proc. 18th World Congress of the International Federation of Automatic Control (IFAC) (2011)

(24) R. Antonello, A. Cenedese, and R. Oboe: "Active damping applied to HSM-driven mechanical loads with elasticity", In Proc. 18th World Congress of the International Federation of Automatic Control (IFAC) (2011)

(25) R. Antonello, A. Cenedese, and R. Oboe: "Suppression of vibration due to transmission error of harmonic drives using peak filter with acceleration feedback", In Proc. IEEE Industrial Electronics Conference IECON 2011 (2011)

(26) C.-C. Wang and M. Tomizuka: "Sensor-based controller tuning of indirect drive trains", In Advanced Motion Control, 2008. AMC '08. 10th IEEE International Workshop on, pp.188–193 (2008)

(27) C.-H. Han, C.-C. Wang, and M. Tomizuka: "Suppression of vibration due to transmission error of harmonic drives using peak filter with acceleration feedback", In Advanced Motion Control, 2008. AMC '08. 10th IEEE International Workshop on, pp.182–187 (2008)

Roberto Oboe (Non-member) was born in Lonigo, Italy, on October 26, 1963. He received the Laurea degree (cum laude) in electrical engineering and the Ph.D. degree from the University of Padova, Padova, Italy, in 1988 and 1992, respectively. He is presently Associate Professor of Automatic Control at the Department of Management and Engineering of the University of Padova, Vicenza, Italy. His research interests are in the fields of applied digital control, telerobotics, haptic devices, rehabilitation robots and applications and control of MEMS.

Davide Pilastro (Non-member) was born in Thiene, Italy, on December 8, 1988. He received the B.E., M.E. in mechatronics engineering from University of Padova, Padova, Italy, in 2010 and 2012, respectively. Currently, he is a Ph.D. student on mechatronics and product innovation engineering in the Department of Management and Engineering (DTG), University of Padova. His research interests include rehabilitation robotics, sensor fusion, and motion control.

Riccardo Antonello (Non-member) was born in Castelfranco Veneto, Italy, on March 13, 1977. He received the Laurea degree (cum laude) in Computer Engineering and the Ph.D. degree in Automatic Control from the University of Padova, Italy, in 2002 and 2006 respectively. From 2006 to 2010 he has been a research associate at the Dept. of Mechanical and Structural Engineering, University of Trento, Italy. From 2010, he joined the Dept. of Management and Engineering, University of Padova. His current research interests lie in the areas of control systems, system identification and mechatronics.

Kazuaki Ito (Senior Member) was born in Mie, Japan, on May 20, 1975. He received the B.S., M.S. and Ph.D. degrees in electrical and computer engineering from Nagoya Institute of Technology, Nagoya, Japan, in 1998, 2000, and 2003 respectively. In 2003, he joined the Department of Electrical and Electronic Engineering, National Institute of Technology, Toyota College, Toyota, Japan, where he is currently an Associate Professor. His current research interests are applications of control techniques to mechatronic systems and haptic devices. Dr. Ito is a member of the Institute of Electrical and Electronics Engineers, the Japan Society for Precision Engineering, and the Society of Instrument and Control Engineers.